RESEARCH ARTICLE

VOLCANICA

A cross-comparison of thermal infrared versus ultraviolet ground-based retrievals of SO_2 masses during Strombolian explosions

Elisabetta Del Bello *[α], Emanuela Bagnato†[α], Lorenzo Guerrieri[β], Giancarlo Tamburello[γ], Stefano Corradini[β], Luca Merucci[β], Francesco Pennacchia[α], Piergiorgio Scarlato[α], Dario Stelitano[β], and Jacopo Taddeucci[α]

[α] Istituto Nazionale di Geofisica e Vulcanologia (INGV) Sezione di Roma1, Roma, Italy.
[β] Istituto Nazionale di Geofisica e Vulcanologia (INGV), Osservatorio Nazionale Terremoti, Roma, Italy.
[γ] Istituto Nazionale di Geofisica e Vulcanologia (INGV), Sezione di Bologna, Bologna, Italy.

Submitted: 2025-04-09 | Accepted: 2025-11-10 | Published: 2025-12-xx

Editor: T. Pering | Typesetter: J. Farquharson

Abstract

This study investigates sulfur dioxide (SO_2) emissions from Stromboli's explosive activity using ground-based remote sensing techniques. We analyze the SO_2 mass derived from ultraviolet (UV) and thermal infrared (TIR) cameras, alongside explosion parameters and emitted products obtained from high-frequency thermal imaging. Our dataset (May 23–24, 2023) includes 49 explosions ranging from gas-dominated (Type 0) to bomb-dominated (Type 1) and ash-rich (Type 2). During non-explosive periods, UV and TIR SO_2 masses are generally comparable, whereas explosions show systematic TIR overestimation relative to UV. The TIR/UV deviation scales with plume temperature and eruption type, reflecting TIR sensitivity to thermal radiation and ash scattering, while UV retrievals remain largely temperature-independent. Our results emphasize the need for temperature-based corrections in TIR retrievals, and support integrated multi-sensor approaches for robust, real-time monitoring of volcanic gas emissions.

Article in Press

Keywords: Cyberinfrastructure; FAIR science; Cloud computing; Numerical models; Volcanology.

1 Introduction

Satellite based remote sensing, operating in the ultraviolet (UV) and thermal infrared (TIR) spectral regions, is well established for volcanic monitoring [Prata and Grant 2001; Watson et al. 2004; Corradini et al. 2010; Coppola et al. 2016; Marzano et al. 2018; Corradini et al. 2021]. Space-based UV and TIR sensors have been successfully used to detect and retrieve the two-dimensional distribution of SO_2 in volcanic plumes [Corradini et al. 2021], yet discrepancies between these estimations require further investigation.

On the ground, UV cameras have been widely employed to monitor volcanic gas emissions ranging from fumarolic activity [Tamburello et al. 2011; 2012; Aiuppa et al. 2023] to persistent open-vent degassing [Barnie et al. 2015; Delle Donne et al. 2017]. Operating typically at a temporal resolution of ~1 Hz, these systems are well-suited for tracking passive degassing and are generally adequate for monitoring plume evolution and estimating the associated gas flux, but they may lack the temporal fidelity required to capture the rapid dynamics of explosive eruptions, particularly during the first seconds, when the highest velocities occur. Conversely, ground-based TIR cameras—commonly used to monitor explosive activity [Patrick et al. 2007; Sahetapy-Engel and Harris 2009; Gaudin et al. 2017; Mereu et al. 2023; Rowell et al. 2023]—have only recently been proposed as tools for SO_2 retrieval [Prata et al. 2024; Guerrieri et al. 2025]. Such studies have introduced low-cost thermal imaging systems and accompanying radiative transfer models capable of estimating plume geometry, velocity, and SO_2 column, marking an important step toward integrating TIR technology into volcanic gas monitoring.

Both UV and TIR cameras measure SO_2 in volcanic plumes along an optical path from the ground. However, each technique is subject to different sources of error and noise. A key advantage of TIR cameras is their ability to operate continuously, while UV cameras are limited to daylight conditions but offer higher sensitivity. This feature is well-known for satellite UV sensors such as Sentinel-5P TROPOMI, which detect SO_2 with roughly thirty times higher sensitivity than multispectral TIR sensors [Corradini et al. 2021]. Additionally, the presence of volcanic ash in the plume introduces systematic biases: UV-based SO_2 retrievals tend to be underestimated due to ash-induced absorption and scattering [Varnam et al. 2021], whereas TIR measurements can be overestimated, particularly during ash-rich eruptions [Corradini et al. 2009; Kearney and Watson 2009]. In addition to ash-caused biases, TIR-based SO_2 retrievals are particularly sensitive to plume-background thermal contrast which can lead to significant overestimation [Prata and Bernardo 2009; 2014; Lopez et al. 2015]. Given these limitations, a systematic intercomparison of the two techniques is crucial for improving our understanding of SO_2 retrieval discrepancies.

We conducted a field campaign on May 23–24, 2023, at Stromboli volcano using a synchronized multi-camera system to investigate SO_2 emissions across a range of eruptive styles. With its combination of continuous passive degassing and frequent explosive activity, Stromboli provides an ideal natural laboratory for testing SO_2 retrieval methods using UV and TIR cameras. Most SO_2 release occurs within the first few seconds of an explosion, with an average degassing duration of ~8 seconds [Delle Donne et al. 2017; Taddeucci et al. 2018], making it challenging to capture key processes such as the arrival of multiple gas pulses [Taddeucci et al. 2012; 2023].

* elisabetta.delbello@ingv.it
† emanuela.bagnato@ingv.it

During the campaign, we measured the SO_2 mass above the crater terrace over time during both quiescent and explosive phases using UV and TIR imaging, incorporating a scientific-grade thermal infrared camera to detect thermal anomalies with high spatial and temporal resolution. This integrated setup enabled a detailed characterization of the relationship between explosive dynamics and degassing behavior. The main objective was to compare UV and TIR signals to test the response of the two techniques in quantifying SO_2 mass across different explosive conditions (e.g. ash-rich versus ash-poor eruptions, passive degassing).

2 Case study

Stromboli has long been an ideal site for studying various gas release modes and rates from active volcanoes, making it a key location for multiparametric field experiments on basaltic explosive volcanism. The volcano exhibits a range of degassing styles, including mild-to-moderate Strombolian explosions, persistent passive degassing, and rhythmic gas puffing [Harris and Ripepe 2007], occurring on the summit crater terrace (~750 m a.s.l., Figure 1A). The frequency, style, and intensity of these explosions can vary significantly over short time scales, ranging from 1 to several explosions per hour [Patrick et al. 2007]. High-energy major explosions (1–10 per year) or paroxysmal events (1–3 per decade) can also occur over longer periods [Andronico et al. 2021]. During the experiment, the three instruments, i.e. the SO_2 retrieving UV and TIR cameras plus the high frequency FLIR camera (Table 1), were co-located at ~400 m elevation along the NE flank of the Sciara del Fuoco, offering a direct view of the active crater terrace (~1023 m away, Figure 1A–1C). In the observation period, explosions occurred from one vent in the NE crater and two vents in the SW crater area. This study focuses on the SW vents, designated as S1 and S2 (Figure 1A).

3 Methods

Over a total ~5 hours of overlapping observations, 49 explosions were recorded, providing a valuable dataset for comparing UV and TIR SO_2 retrievals in an explosive degassing context. The images obtained were synchronized with GPS. To enable point-by-point comparison across datasets, the higher-frequency UV (10 Hz) and FLIR (30 Hz) time series were resampled to match the 0.5 Hz acquisition rate of the TIR data. This was achieved using `MATLAB`'s `retime` function with the `nearest neighbor` method, ensuring temporal alignment without applying any smoothing.

For the retrieval of SO_2 mass, we deliberately opted to use a fixed region of interest (ROI) positioned directly above the crater vent Figure 1D), consistently applied across both instruments, and integrating SO_2 column densities within this ROI to obtain the total SO_2 mass per frame. This approach was chosen to ensure a synchronous, spatially aligned comparison between the two techniques, minimizing discrepancies and avoiding assumptions about plume dynamics. The ROI location was also dictated by practical constraints, like the limited field of view of the UV camera and the short-lived, relatively low-magnitude nature of the investigated explosions, which dissipate rapidly and become harder to detect with distance. Placing the ROI close to the vent maximizes SO_2 signal detectability for the UV system. An alternative method often used in volcanic gas studies involves computing the SO_2 flux by integrating the column amounts across a transect located perpendicular to the plume and multiplying by an assumed plume velocity to obtain the mass. However, while this approach can provide time-resolved flux series, it was not suitable for our objective of comparing retrieval techniques under controlled and comparable conditions. In our case, it would have introduced substantial additional uncertainties, most notably from the assumptions required for plume velocity and from spatial and temporal mismatches between instruments. Table 1 summarizes the main characteristics of the UV, TIR and FLIR ground based systems used during the field campaign.

3.1 UV camera

This study employs a portable, manually operated dual UV camera system made up of two Thorlabs 340UV-GE cameras (Figure 1C) that are mounted closely together on a rail and supported by a tripod (a similar setup is detailed in Kantzas et al. [2010] and Tamburello et al. [2011, 2012]. This UV camera model supports high-frequency data capture of up to 50 Hz, enabling the detection of gas variations during explosive events. The two CCD (Charge-Coupled Device) cameras come equipped with a 1/3" format sensor featuring 640 × 480 pixels (320 × 240 following vertical and horizontal binning), with pixel dimensions of 7.4 × 7.4 µm and a 14-bit digital output via gigabit ethernet. Each camera has 25 mm quartz lenses and bandpass filters centered at 310 and 330 nm. The 310 nm filter captures SO_2 absorption, while the 330 nm filter measures wavelengths outside the absorption bands, allowing for a qualitative measure of absorbance (A) per pixel as:

$$A = -\log_{10}\left(\frac{IP_{310}/IB_{310}}{IP_{330}/IB_{330}}\right) \quad (1)$$

where IP and IB represent the pixel intensity values of the dark-subtracted plume and background sky images, respectively, with filters applied. This calculation produces an offset in the absorbance from the clear sky in the absence of SO_2. This value is captured during processing, and the mobile mean is subtracted from each image to correct the offset. The UV camera system is calibrated every hour between measurement sequences, using gas cells of known SO_2 slant column densities (SCD of 208, 1000, 2000 ppm·m) placed in front of the camera, and more often when lighting conditions change rapidly. The known SCD are plotted versus A, and the slope and intercept derived from the best fit line are used to convert absorbance values to ppm·m for each pixel. Data acquisition is managed by custom `LabVIEW` code, while image processing is performed post-acquisition using custom `Python 3` code. Preprocessing included image alignment to correct for shifts between the two simultaneously operating UV cameras, establishing calibration coefficients, and choosing a clear sky background area. It is important to note that during the image alignment and merging procedure, part of the NE crater region lies at the edge of the overlapping fields of view and is partially cut out in the resulting merged absorbance image. For

–Article in Press–
–Article in Press–

Table 1: Main characteristics of the UV, TIR, and FLIR ground based systems used during the field campaign.

	Image resolution (Pixel)	Focal length (mm)	Pixel size* (m)	Hfov*† (m)	Vfov*† (m)	Frame rate (Hz)	Camera tilt‡ (°)
TIR	320 (H) × 240 (V)	4	3.2–4.1 (H) 3.3-8.1 (V)	1118	1132	0.5	30
UV	640 (H) × 480 (V)	24	0.6-0.6 (H) 0.7–0.9 (V)	192	216	10	20
FLIR SC655	640 (H) × 480 (V)	41.3	0.41(H) 0.44 (V)	265	230	30	20

* At vent distance (measured by laser rangefinder);
† Full frame;
‡ Above horizontal.

–Article in Press–

this reason, emissions from the NE crater were not included in the quantitative analysis, even though partial signals from NE activity are still visible in the time series (Figure 4). The total SO_2 mass in the ROI within each frame is quantified by integrating the SCD over the selected image area [Tamburello et al. 2012]. Pixel dimensions at the vent are calculated based on the horizontal and vertical distances between the plume and cameras (measured by laser rangefinder), its inclination, the field of view (FOV) of the lenses, and the number and size of pixels in the detector.

While UV cameras provide high temporal resolution for detecting short SO_2 bursts during Strombolian explosions, several factors can affect data accuracy. One primary source of error is the presence of ash and aerosols in the plume, which cause absorption and reflection at the cloud's surface [Kern et al. 2010]. Throughout the acquisition, atmospheric conditions remained relatively clear, and the plume was never optically thick, except during the initial phase of ash-rich Strombolian explosions. Although it was not possible to precisely quantify the error introduced by ash interference, we minimized its impact by using the FLIR thermal camera to accurately identify the onset time of each explosion. This allowed us to select SO_2 mass values from the UV camera data prior to any significant ash emission, ensuring that the retrieved UV signal was not affected by ash-related absorption or scattering (negative peak in Figure 2D). Another factor is given by plume orientation with respect to the FOV. While ash particles quickly settle, making the plume more transparent as it ascends, the assumption that each pixel represents an equal distance from the camera is inaccurate if the plume is moving closer or farther. The positioning of the measurement site and varying sunlight angles introduce uncertainty in SO_2 mass estimates, primarily due to light dilution from photon scattering into the camera's field of view. The distance from the plume is the dominant factor controlling this effect, as shown by Campion et al. [2015], who reported underestimations of up to 25 % at a distance of around 2.0 km. The close proximity of the UV camera to the crater rim and volcanic flanks made it difficult to correct for light dilution caused by reflected UV light on the rocky background at varying distances [Campion et al. 2015]. Taking into account a reported 25 % underestimation at 2 km [Campion et al. 2015] and a reported 10 % error at 500 m [Delle Donne et al. 2022], we estimate the uncertainty at our 1 km measurement distance to lie between these values. Furthermore, based on estimates from comparable systems at Stromboli (Lo Bue Trisciuzzi et al. [2024], following Kern et al. [2010]), the SO_2 camera system can be estimated to have a total uncertainty on the order of 30 %.

–Article in Press–

3.2 TIR camera

The novel TIR ground based camera system VIRSO$_2$ has been developed in the sphere of the ESA-VISTA project* by AIRES ltd. company. The system consists of three cameras: one visible, one TIR broadband (7.8–14 µm, BB) and another similar TIR broadband with a narrowband filter in front (centered at 8.7 µm, NB) [Guerrieri et al. 2025]. The two TIR BB cameras consist of a 320 × 240 uncooled microbolometer detector array (manufactured by SEEK Thermal, MOSAIC Core C3 Series, see Prata et al. [2024]) with a FOV of 56° × 42°, with a 12 µm pixel size. The overall system is extremely portable (Figure 1B), relatively low-cost, and has an actual power consumption of ~15 Wh. Its ability to be used both day and night can make it a very important tool for the continuous and real time monitoring of volcanic emissions from the ground. The full details of the new system are given in Guerrieri et al. [2025]. Here we synthetically describe the approach used to retrieve SO_2 column amounts from the infrared spectra. The presence of the NB filter, essential for SO_2 retrieval, introduces two main issues that require correction: (1) a circular optical artifact known as the *ghost image*, and (2) the loss of the factory temperature calibration of the sensor (Supplementary Material 1 Figure S1A). The ghost image occurs because the interference filter is not perfectly transmissive, causing reflections of hot components behind the filter onto the detector. To correct for this, a custom-built uniform-temperature blackbody target is placed close to the camera, filling the entire field of view. While the ghost is present in this calibration image, its uniform background makes it easily identifiable and removable. The extracted ghost signal is then subtracted from all crater-facing scenes. The second correction addresses the re-calibration of the NB images, which are primarily influenced by the filter temperature rather than the scene temperature. Calibration is based on a linear relationship derived from two plume-free reference points in the BB and NB im-

*https://eo4society.esa.int/projects/vista/

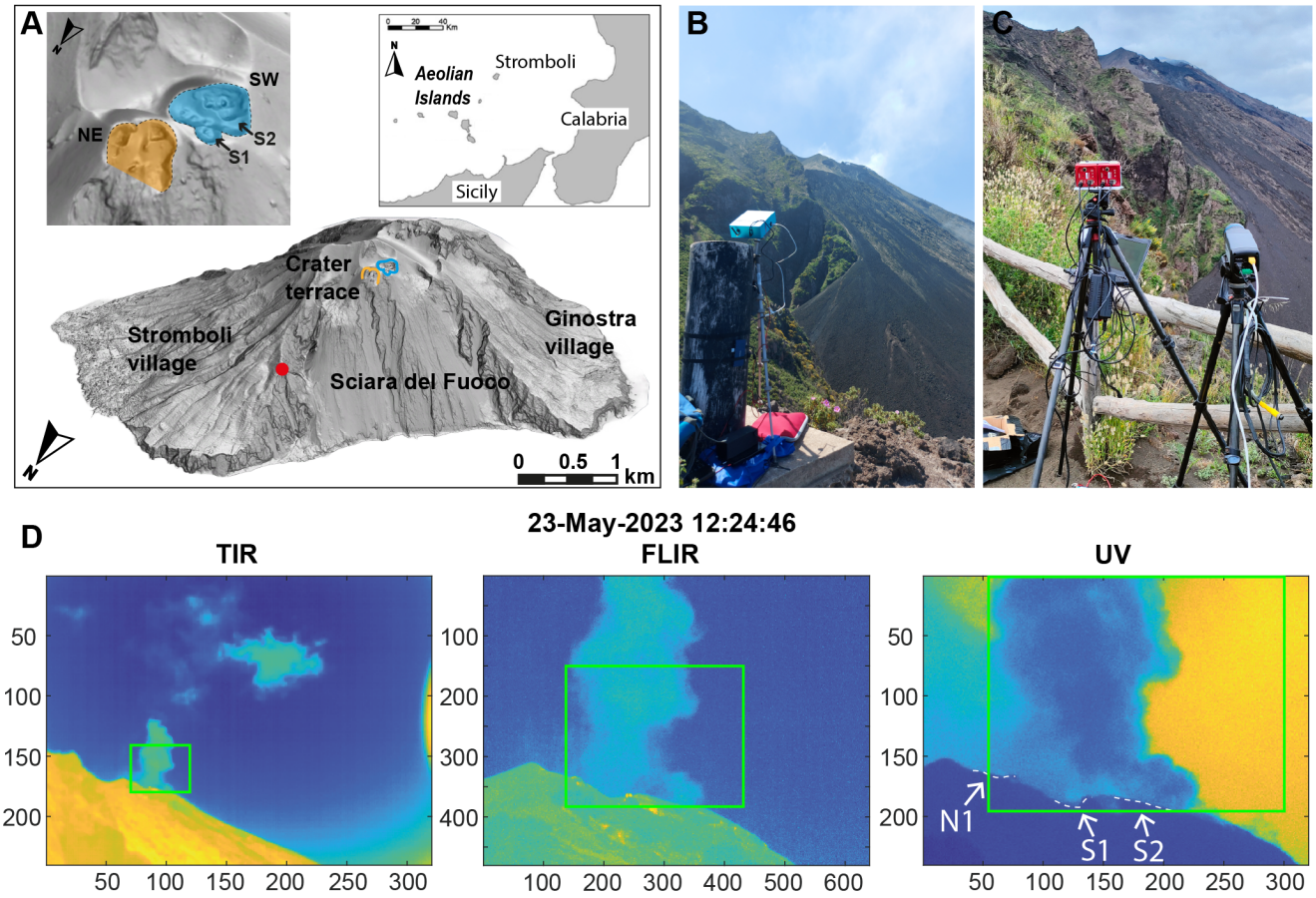

Figure 1: [A] Geographic location of Stromboli and its high-Resolution SfM Topography obtained on 22–23 May 2023 [Civico and Ricci 2024], showing the measurement site (solid red point) positioned at an elevation of approximately 400 m a.s.l., and at a distance of 1023 m from the active vents. The left inset shows a detail of the NE (orange) and SW (cyan) crater areas, and the location of the S1 S2 vents. Field deployment of TIR [B] and UV camera-FLIR system [C] imaging instruments in line of sight to the active crater terrace. [D] Synchronized still frames from TIR, FLIR, and UV recordings of an explosion at 12:24:46 23 May, 2023. FLIR and TIR panels display temperature variations, while UV panel shows the image captured at 310 nm The ROI is the green box. The position of the active vents S1 and S2 (SW crater) and N1 (NE crater, excluded from analysis) is also shown. Axis units are in pixels, and the size of the field of view of the images is provided in Table 1.

ages, typically the clear sky and the ground, chosen to span a wide temperature range. Assuming the BB temperatures (Supplementary Material 1 Figure S1B) as reference, the calibrated NB temperatures for these points are obtained from radiative transfer model (RTM) simulations that account for the camera geometry and the environmental conditions. After ghost removal and BB re-calibration, we obtain a corrected 8.7 µm temperature image (Supplementary Material 1 Figure S1C). The third step involves computing a temperature difference image (DT) by subtracting a clear-sky reference image from the corrected NB image (Supplementary Material 1 Figure S1D). This is the main information content of the retrieval scheme, because the difference between the 8.7 µm temperature inside and outside the plume depends on the SO_2 emission and consequently from its density. Similar DT values are also obtained from RTM simulations varying the SO_2 vertical column density (VCD) and the elevation angles (θ) of the pixels of the TIR camera (Supplementary Material 1 Figure S1E). Moreover, because also the clear air temperatures are not uniform, and increase as the θ angle decreases, it is necessary to consider a "zero value" for each row of the image. It is possible to simply consider the smoothed row by row minimum values of the overall image or, alternatively, it is also possible to use the clear sky temperatures simulated with the RTM model.

Finally, the comparison of the simulated and measured NB DT gives, by linear interpolation, the SO_2 content (Supplementary Material 1 Figure S1F, which is then turned into SCD by considering the elevation angles of each pixel (i, j) of the image (Equation 2):

$$\mathrm{SCD}_{i,j} = \mathrm{VCD}_{i,j} / \sin\theta_{i,j}. \quad (2)$$

The SO_2 mass (M_s) is then computed by multiplying the SCD with the camera pixel area (Equation 3).

$$M_s = \sum_{i,j} \mathrm{Area}_{i,j} \cdot \mathrm{SCD}_{i,j}. \quad (3)$$

–Article in Press–

In this work, the MODerate resolution atmospheric TRANsmission (MODTRAN) 5.3 [Berk et al. 2005] simulations were performed using pressure, temperature and humidity (PTH) vertical atmospheric values obtained from European Centre for Medium-Range Weather Forecasts (ECMWF) Reanalysis v5 (ERA5) dataset [Hersbach et al. 2023] on 24 May 2023 00 UTC, at Latitude = 38.75N and Longitude = 15.25E.

The different calibration steps and procedure inputs induce several possible sources of error, not all easily computable. To reduce the background error, the average SO_2 SCD value of a 40×40 pixel area outside the plume was computed and subtracted to the retrieval. Other sources of errors, related to the uncertainties of the input parameters, are easier to estimate. In Guerrieri et al. [2025] a sensitivity study was performed considering the uncertainties of the distance and thickness of the plume, the PTH atmospheric values, and the central elevation angle of the camera giving an overall error of about 35 %. Finally, two other important sources of error must be considered for the measurements carried out in this study, involving explosive activity. The first is related to the presence of ash which, as the SO_2 content, affects the NB channel increasing the apparent 8.7 µm temperature of the plume (the particles emit across the entire TIR spectrum) [Watson et al. 2004; Kearney et al. 2008; Corradini et al. 2009; Kearney and Watson 2009; Corradini et al. 2010]. In this study, MODTRAN simulations were performed assuming plumes containing only SO_2 and no ash. Thus it is anticipated that the presence of ash during the measurements will be misinterpreted by the retrieval algorithm as additional SO_2, leading to an overestimation of the TIR-derived values. The second is related to the fact that the chosen ROI close to the vent implies a thermal contrast between the higher temperature plume and the background, which is not considered in the RTM simulations (where the plume is assumed in thermal equilibrium with the surrounding air temperature).

3.3 FLIR camera

The thermal infrared camera (FLIR SC655, Figure 1C) acquired high frequency videos of the explosive activity at 30 Hz, and at a spatial resolution of 640 × 480 pixels per image (Figure 2A–2B). Thermal images were corrected for the atmospheric absorption through the software after air temperature (20 °C), humidity (50 %), emissivity (0.92) and target distance input (1023 m), and then scaled by knowing pixel size (17 µm), lens focal length (41.3 mm), distance (1023 m), and dip angle of the camera (20°), obtaining a horizontal and vertical FOV of 265 m and 230 m, respectively (Table 1). Note that since the assumed surface emissivity (0.92) reflects typical values for volcanic particles, the temperatures measured during gas-dominated explosions may be affected by an underestimation, as volcanic gases emit less radiation (emissivity < 0.1). To evaluate this effect, we quantified the expected underestimation due to low emissivity using a simplified Stefan–Boltzmann approach (full derivation in Supplementary Material 2). Our calculation for a gas plume with a true temperature of 600 °C (873 K) and an emissivity of 0.1 shows it would be recorded as an apparent temperature of approximately 228°C (501 K). In consideration of this, the temperatures derived from FLIR data must be regarded as apparent temperatures, and we conservatively estimate a maximum underestimation of ~60 %, for gas-dominated events in our dataset.

Thermal infrared video analysis was carried out using custom-built MATLAB algorithms [Gaudin et al. 2017] to extract: (1) the mean ROI temperature anomaly (i.e. after subtraction of the background temperature) over time, calculated as the average of all pixel values within the ROI; and (2) kymographs, which display thermal anomalies over time (x-axis) and elevation (y-axis, m), with vertical pixels converted to meters based on camera parameters (Table 1).

Kymographs (Figure 2C–2D) reveal distinct thermal anomalies: bomb-sized pyroclasts show sharp parabolic traces, indicating rise and fallout velocities; ash emissions appear as diffuse streaks with positive slopes; gas emissions manifest as rapidly dissipating transient thermal anomalies. Explosions are quantified by identifying four key points (Figure 2C): explosion onset (P1) and offset (P2) given as first and last pyroclast ejection, maximum pyroclast height (P3), and a point on the initial thermal rise 50 pixels above P1 (P4). From these points coordinates, where x is time and y is vertical position in meters, we define: duration as $(x_2 - x_1)$, inter-event time as the time between onsets of explosion i and that of the previous explosion $i-1$: $(x_1(i) - x_1(i-1))$, elevation as $(y_3 - y_1)$, and initial velocity as the slope between P4 and P1, i.e. $(y_4 - y_1/x_4 - x_1)$, representing the average ascent rate of the explosion during the first ~20 m of the column. Vent identification is based on kymograph clustering and thermal video cross-referencing. Explosions are categorized based on eruptive products [Patrick et al. 2007; Leduc et al. 2015; Simons et al. 2020] using visual observations of the kymographs, alongside FLIR original videos: i) Type 1 are ballistic-dominated explosions with clear parabolic trajectories and little to no ash; ii) Type 2a are mixed explosions with significant amount of bombs and ash plumes, overlaying ballistic paths; iii) Type 2b are ash-dominated explosions with few or absent ballistics, forming vertically dispersed, inclined streaks; iv) Type 0 are gas jets with sharp vertical anomalies; lower signals indicate puffing/spattering. To quantify the peak SO_2 masses for each explosion from TIR and UV data, we first identify the explosion onset time (x_1) using thermal images. The explosion's peak mass is then calculated as the difference between the maximum SO_2 value, measured manually for each time series, and the onset time value $(m_2 - m_1$, Figure 2C–2D) . This method effectively isolates the contribution of each explosion, removing the influence of overlapping passive degassing. It also helps reduce errors in UV baseline measurements (m_1) and accounts for temporary UV peak delays caused by elevated ash concentration at the explosion's onset. In our data, choosing the negative minimum instead of the FLIR onset as the reference m_1 value results in a 3–15 % difference in the calculated peak mass relative to the FLIR onset method.

4 Results

4.1 Observed explosive activity by FLIR setup measurements

During the observation period, 49 events were analyzed using FLIR videos to characterize the explosion type. A range of

–Article in Press–
–Article in Press–

–Article in Press–

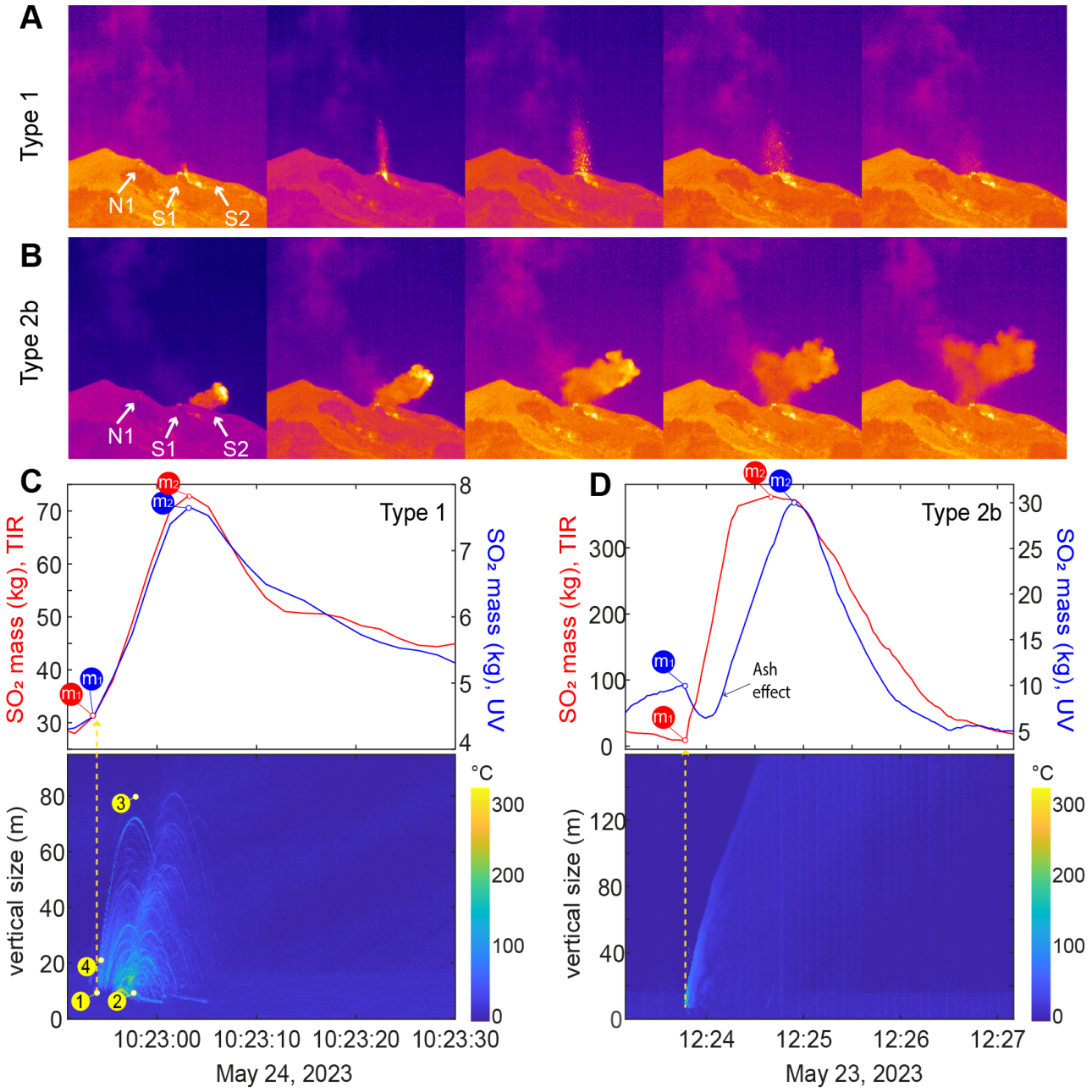

Figure 2: Multiparametric analysis of two explosions at Stromboli on May 23, 2023. [A–B] FLIR thermal infrared images of a Type 1 explosion at vent S1 (10:58:50) and a Type 2b explosion at vent S2 (11:01:21), with 2 s and 4 s frame intervals, respectively. N1 vent (NE crater, excluded from analysis) is also shown. [C–D] Examples of Type 1 and Type 2b explosions. Top panels show SO_2 mass time series from UV (blue) and TIR (red) data. For each explosion, the peak SO_2 mass is calculated subtracting the onset value (1) from the maximum value (2). Note the different left- and right-hand y-axes. In ash-rich explosions (panel [D]), the UV signal exhibits a temporary negative peak , due to initially high ash concentration, which delays the SO_2 maximum. Bottom panels show FLIR-derived thermal anomaly kymographs (in °C), shows volcanic ballistic projectiles during the Type 1 explosion and the ash plume rising during the Type 2b explosion. In [C], the 4 points used to extract the explosion parameters are indicated.

explosion types was recorded, from gas-only bursts (Type 0) to those dominated by bombs (Type 1) or ash (Type 2), ejecting varying proportions of lapilli- to bomb-sized pyroclasts. Over the two days, Type 1 explosions were the most frequent (67 %), followed by Type 2b (14 %), Type 0 (12 %), and Type 2a (6 %) (Table 2). Explosions from S1 were more frequent, clustered around moderate heights (~30–55 m) and shorter durations (~2–3 s), predominantly Type 1 and secondarily Type 0. In contrast, S2 explosions were more variable, ranging from ~0–40 m in height and ~2–9 s in duration, displaying a wider range of explosion types (Figure 3). Type 0 explosions were the weakest, with short durations (<2 s) and low heights

(<20 m). Type 1 explosions clustered at 40–55 m and 2–5 s, although covered a wide range of heights (10–80 m) and durations (<10 s), while Type 2a and 2b lasted longer, with the latter displaying lower elevations (~0–40 m). Type 0 explosions remained low (~10–30 m) and brief. Higher explosion velocities (~20–40 $m\,s^{-1}$), representing the average initial ascent rate of the pyroclast jet, generally corresponded to Type 1 events, while Type 0 and 2a explosions had lower velocities (<20 $m\,s^{-1}$), reflecting weaker gas and ash jetting. Most explosions recurred within 1–10 minutes, with some events exhibiting up to 18 minutes inter-event time.

4.2 Comparing UV with TIR SO2 retrievals

The SO_2 mass time series from TIR and UV data processing exhibit synchronized, sharp variations in signal amplitude in correspondence to the onset of explosive events, as indicated by fluctuations in the mean ROI temperature of thermal images (Figure 4). The data captured changes in explosion type, frequency, and passive degassing over the two days. Overall, during explosive periods, TIR dataset shows significantly higher signal amplitudes compared to UV measurements. Type 1 explosions are characterized by short-lived peaks in TIR and UV signals, whereas Type 2 explosions—particularly Type 2b—are associated with higher SO_2 peaks, especially in the TIR signal. During these events, the UV signal often shows a negative peak followed by a delayed maximum relative to TIR (e.g. Figure 2B).

During non-explosive periods, SO_2 emission remains relatively steady, and the variations observed suggest a contribution from passive degassing or smaller-scale active degassing that is not captured by the FLIR camera. Additionally, some fluctuations result from activity in the NE area, which lies outside the investigated field of view (Figure 4). The mean ROI temperature remains stable throughout both observation periods, with minor fluctuations that may reflect variations in background thermal intensity.

The point-by-point comparison of SO_2 time series from the two methods, combining data from both 23 and 24 May 2023 (Figure 5A) shows a weak overall correlation (Pearson correlation coefficient R = 0.32) over the full ca. 5-hour dataset. A rolling correlation analysis (Figure 6), performed using 100 s windows with 2 s steps, shows a marked improvement, with $R > 0.7$ in 47 % of the windows. When both TIR and UV time series are smoothed over 50 samples (≃100 s) before applying the rolling correlation, the agreement further increases, with $R > 0.7$ in 60 % of the windows.

In terms of absolute mass values detected, a distinction emerges between explosive and passive degassing conditions. During explosive periods (shaded bands in Figure 4, orange crosses in Figure 5), the interquartile range (IQR) of TIR-derived SO_2 masses spans from 16 to 52 kg (median: 32 kg), whereas UV retrievals yield much lower values, ranging from 6 to 15 kg (median: 9 kg). In contrast, during non-explosive periods (data outside the shaded bands in Figure 4, blue crosses in Figure 5), the two datasets provide closer values, with TIR values ranging from 0.9 to 7.5 kg (median: 2.7 kg), and UV values ranging from 3.4 to 6.8 kg (median: 5.0 kg), accounting for ~70 % of the total dataset. The TIR/UV mass ratio further illustrates this bias: during explosive events, TIR exceeds UV by a median factor of ~3.2 (IQR: 1.7–7.4; vertical box chart in Figure 5B). While most explosive data fall within this range, a small subset (<8 %) represents outliers, reaching 15–280 times UV values.

When the TIR/UV SO_2 mass ratio is examined as a function of the mean ROI temperature recorded by FLIR a slightly improved correlation emerges (R = 0.46, Figure 5B), showing that the TIR/UV ratio increases linearly with mean ROI temperature. This trend reflects the evident TIR dependence on the mean ROI temperature (R = 0.57, Figure 5C) instead of the UV showing negligible correlation (R = 0.1, Figure 5D). During explosive periods the mean ROI temperatures have IQR values between 1.6 and 5.1 °C. Conversely, during passive degassing the median TIR/UV ratio is <1 (0.6; IQR: 0.2—1.5) and the mean ROI temperatures are lower (IQR: 0.8–2.0 °C).

We next focus on individual explosions for which the vent, eruption type, and associated eruptive parameters have been characterized. The SO_2 explosion's peak masses from TIR and UV measurements span 0.6–421 kg and 0.5–33 kg, respectively (Figure 7A and Table 2). Explosions from the S2 vent release higher SO_2 masses than S1, with broader IQR and higher median, particularly in the TIR-derived data. However, the influence of the eruptive vent cannot be evaluated separately, as vent S1 is almost exclusively associated with Type 1 explosions.

Median SO_2 mass increases from Type 0 to 1 to 2a and 2b events in both datasets. With the exception of the Type 2b explosions, which show the largest deviations in the TIR data, variability remains comparable across the other types. The statistical significance of some distributions, however, is limited by the small number of analyzed events (e.g. only three Type 2a explosions).

Notably, for the ash-dominated Type 2b events, TIR masses exceed UV by a median factor of 22 (Figure 7B). Other types (0, 1, 2a) show lower median factors, ranging 2–7. Excluding Type 2a, whose statistical robustness is limited, a correlation emerges between median TIR/UV ratio and median ROI temperature (Figure 7B), allowing classification into two distinct groups: Type 1 and 2b explosions, with high TIR/UV ratios, correspond to bomb- and ash-rich, high-emissivity plumes where apparent temperatures approximate true source temperatures. Type 0 explosions with low TIR/UV ratios, are indicative of gas-dominated, low-emissivity conditions where apparent temperatures substantially underestimate true values.

5 Discussion

5.1 Comparative performance of TIR and UV SO_2 retrievals

Our measurements were acquired using the same field of view and target distance, excluding geometric effects as a source of discrepancy. The generally low correlation between UV and TIR SO_2 measurements over the full time series (R = 0.32; Figure 5A) therefore reflects the transient, heterogeneous nature of the vent-proximal plume. Decorrelation arises from the different sensitivities of the two sensors to rapid variations in plume composition and radiative conditions—UV being af-

–Article in Press–
–Article in Press–

Table 2: Statistical distribution of the UV and TIR camera's SO_2 mass data, as shown in Figure 5A (explosive and non-explosive periods) and Figure 7A (individual explosions, grouped by vent and type). Reported values include the median, interquartile range (IQR), and the number of data points for each distribution.

	Number of data	Median SO_2 masses (kg) (IQR)		Median TIR/UV Ratio (IQR)	Median mean ROI Temperature (°C) (IQR)
		UV camera	TIR camera		
Explosions' peak mass (by vent)					
S1	34	2.8 (1.3–5.4)	22.9 (8.8–36.9)	-	-
S2	15	14.6 (8.0–18.4)	125.8 (51.9–273.3)	-	-
Explosions' peak mass (by type)					
0 (gas-dominated)	6 (12%)	2.0 (1.3–14.9)	10.4 (7.2–42.8)	6 (3–7)	4 (3–6)
1 (coarse pyroclasts)	33 (67%)	3.9 (1.6–6.4)	26.3 (12.6–47.1)	7 (3–13)	12 (7–16)
2a (ash-dominated, with ballistic particles)	3 (6%)	11.4 (9.5–14.5)	40.9 (24.9–61.5)	2 (1–8)	6 (5–7)
2b (ash-dominated, with fewer ballistic particles)	7 (146%)	14.6 (11.2–15.0)	278.0 (243.7–340.5)	22 (20–30)	14 (11–28)
Time series data					
Explosive periods	2143	9.4 (5.8–15.1)	32.0 (15.9–51.7)	3.2 (1.7–7.4)	2.7 (1.6–5.1)
Non-explosive periods	4727	5.0 (3.4–6.8)	2.7 (0.9–7.5)	0.6 (0.2–1.5)	1.2 (0.8–2.1)

–Article in Press–

Article in Press–

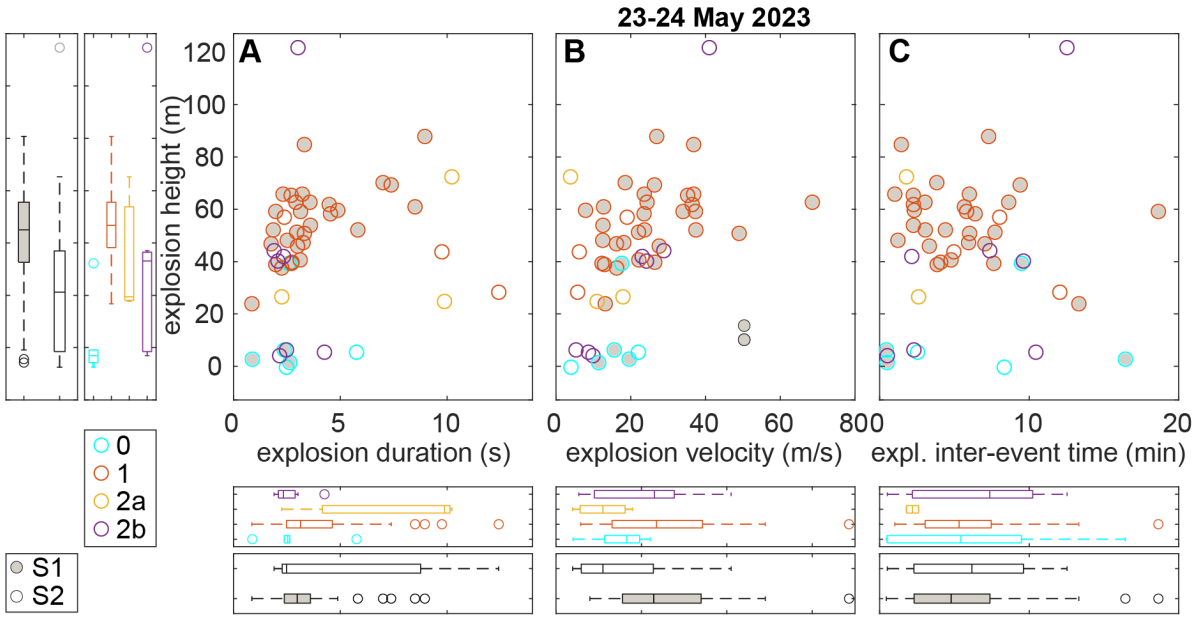

Figure 3: Explosions parameters characterized by FLIR video analysis. The scatterplots show height against [A] duration, [B] velocity, representing the average initial ascent rate, and [C] inter-event time for each explosive event recorded on 23–24 May 2023. Explosions are classified into Types: 0 (gas jet, cyan), 1 (ballistic-dominated, red), 2a (bombs + thick ash plume, yellow), and 2b (ash-dominated, purple). Filled and empty symbols correspond to source vents S1 and S2. Boxplots summarize the distributions for each explosion type. Boxes represent the interquartile range (IQR), whiskers extend to 1.5 × IQR, and outliers are beyond this range.

fected by haze, aerosols, and water droplets, while TIR responds to temperature contrasts and silicate ash. Even small temporal or amplitude offsets resulting from these differential responses can distort signal shapes and misalign peaks between the two datasets (see Figure 2D and Supplementary Material 1 Figure S2). Rolling correlation analysis confirms this interpretation: over short intervals (<2 min), strong positive correlations ($R > 0.7$, Figure 6) occur in nearly half the

–Article in Press–

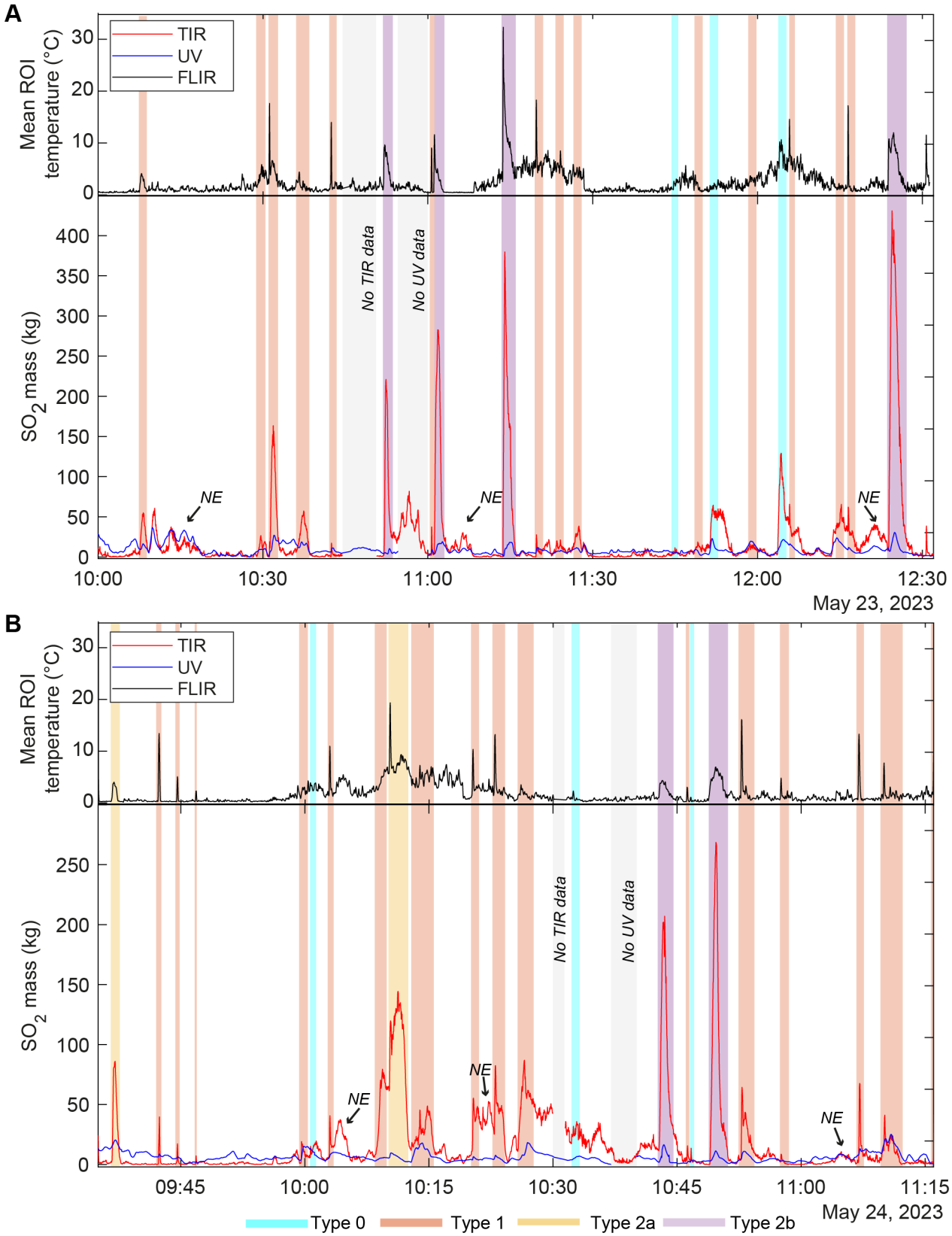

Figure 4: Time series of SO_2 mass (kg), estimated through simultaneous acquisition by UV-camera (blue line), TIR (red line) and temporal variation of the ROI mean temperature anomaly measured by FLIR (black line) acquisition, during [A] 23 and [B] 24 May 2023, respectively. Explosive events and types are also reported: Type 0; Type 1; Type 2a and Type 2b, as indicated by the shaded vertical bands. The non-shaded peaks indicate activity from the NE area that was not included in the investigated FOV. Gaps in TIR and UV data are marked in grey, reflecting periods when measurements were unavailable.

–Article in Press–

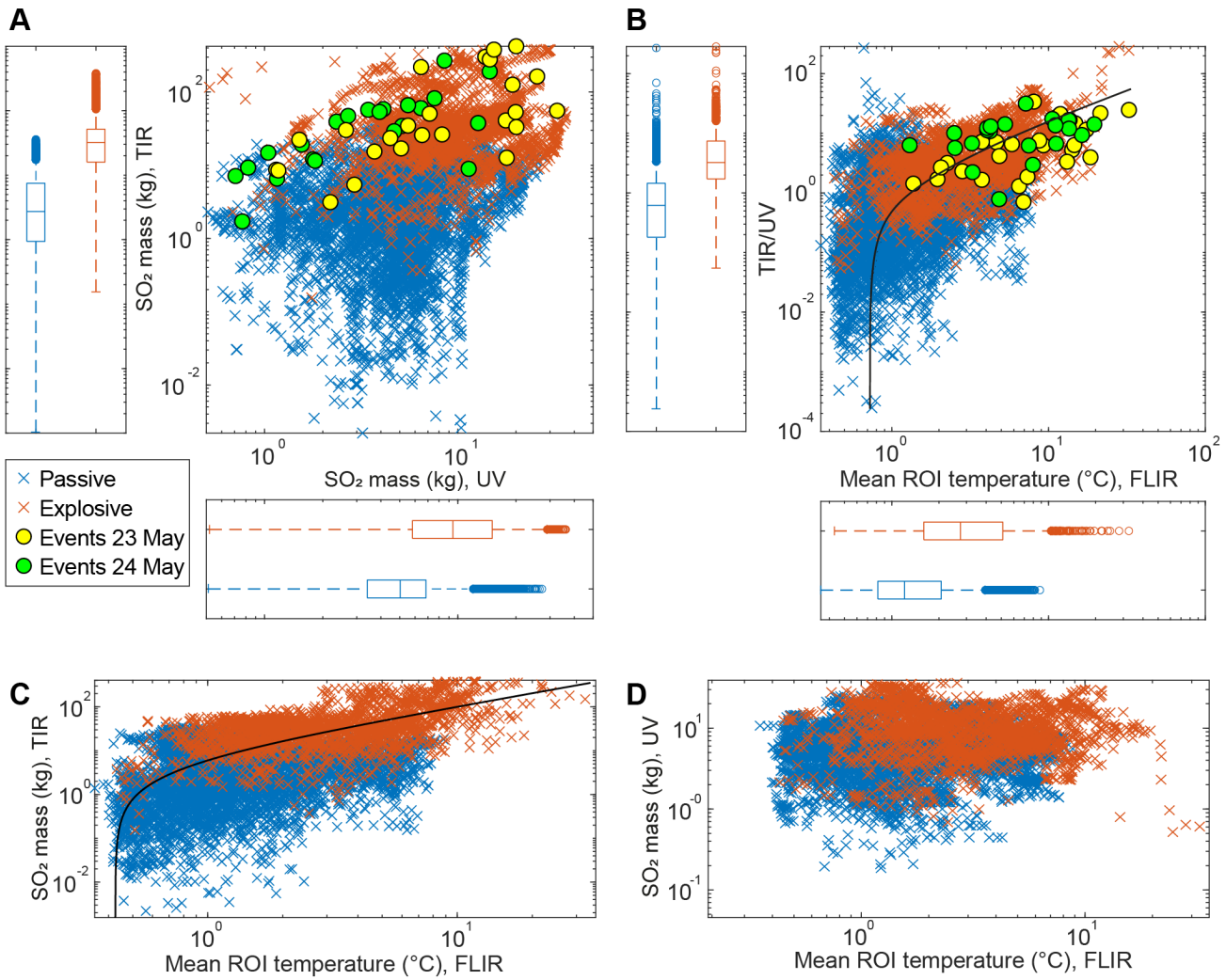

Figure 5: Comparison of SO_2 retrieval techniques using TIR and UV data collected on May 23–24, 2023. [A] Scatter plot showing poor correlation of SO_2 mass from TIR versus UV measurements (R = 0.32), including all data from the two days. Corresponding boxplots highlight distribution differences (see also Table 2). [B] TIR/UV ratio as a function of mean image temperature, showing a positive correlation (R=0.46). [C, D] Relationship between SO_2 mass retrievals and mean ROI FLIR temperature for TIR (R = 0.57) and UV (R = 0.1) measurements, respectively. The solid line in B and C represents the best-fit linear trends. Each cross corresponds to an individual sample from the time series (resampled at 0.5 Hz, as in Figure 4; orange: explosive; blue: passive), and circles indicate explosions' peak SO_2 mass and temperature (yellow: 23 May; green: 24 May) retrieved with the method shown in Figure 2.

cases, increasing to ~60 % after applying a 100-second moving average smoothing. This improvement indicates that high-frequency fluctuations, rather than eruptive state, dominate the decorrelation observed in the raw data. Thus, TIR and UV retrievals provide coherent SO_2 variations over short, stable periods, while long-term decorrelation mainly reflects the integration of rapid, sub-minute plume dynamics.

The two techniques perform differently across degassing regimes (Figure 5). During non-explosive periods, when the plume is cooler and particle-poor, TIR and UV measurements yield comparable SO_2 mass estimates (median TIR/UV ~0.6), corresponding to a mismatch of about 40 % (calculated as 100 × (TIR–UV)/UV). In contrast, during explosions, TIR and UV retrievals diverge significantly (median TIR/UV ~ 3.2, Figure 5 and Table 2), with a median discrepancy of roughly 220 %, indicating that the divergence increases when eruptive material (either ash or incandescent bombs) enters the field of view, and highlighting the strong influence of plume conditions and radiative environment on the agreement between the two techniques.

The positive correlation between the TIR/UV SO_2 mass ratio and the mean ROI temperature (R = 0.46; Figure 5B) further reflects the effect of thermal radiation and scattering by ash and incandescent particles on the TIR signal (Figure 5C), with TIR overestimation scaling with explosion type, corresponding to "cold" versus "hot" FLIR apparent temperatures, which serve as a proxy for gas-dominated versus particle-dominated plumes. High-emissivity, ash-rich plumes and incandescent magma fragments (Type 1) show the greatest off-

–Article in Press–

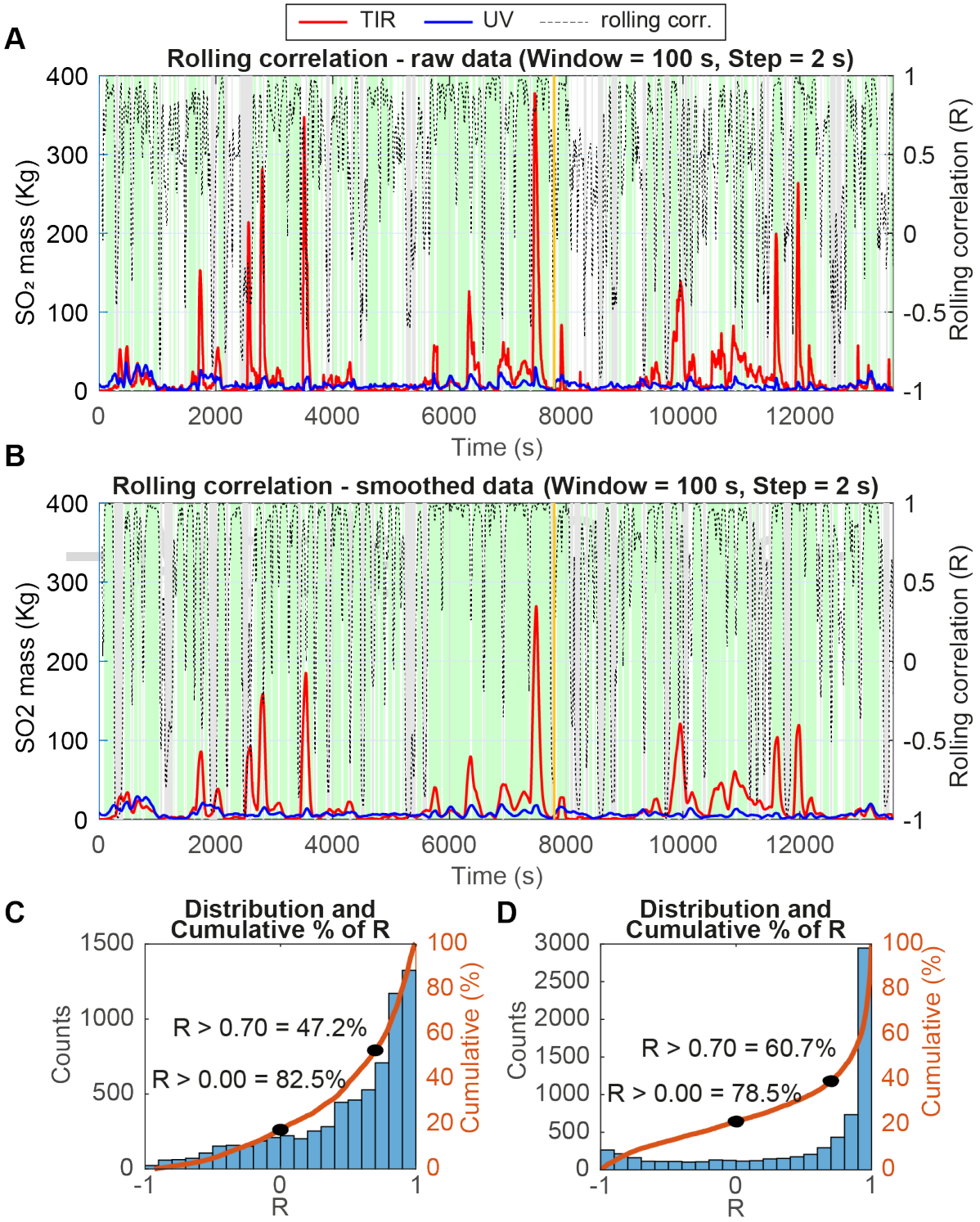

Figure 6: Comparison of TIR and UV SO_2 mass signals and their rolling correlation. [A] Time series of SO_2 masses retrieved from TIR (red) and UV (blue) techniques, with the rolling Pearson correlation coefficient (R, black dashed line) calculated using a 100 s moving window (step = 2 s). Green shading indicates periods of strong positive correlation (R > 0.7), while grey shading indicates anti-correlation (R < 0). The yellow vertical line separates data from 23 and 24 May 2023. [B] The same analysis after applying a 100 s moving average to both signals, which reduces short-term fluctuations and enhances temporal coherence between datasets. [C, D] Histograms and cumulative distributions of R values from panels [A] and [B], respectively. For raw signals, 47.2 % of the data exhibit R > 0.7, and 82.5 % show R > 0. After smoothing, the fraction of highly correlated data increases (R > 0.7 = 60.7 %), while the proportion of positive correlations remains similar (R > 0 = 78.5 %).

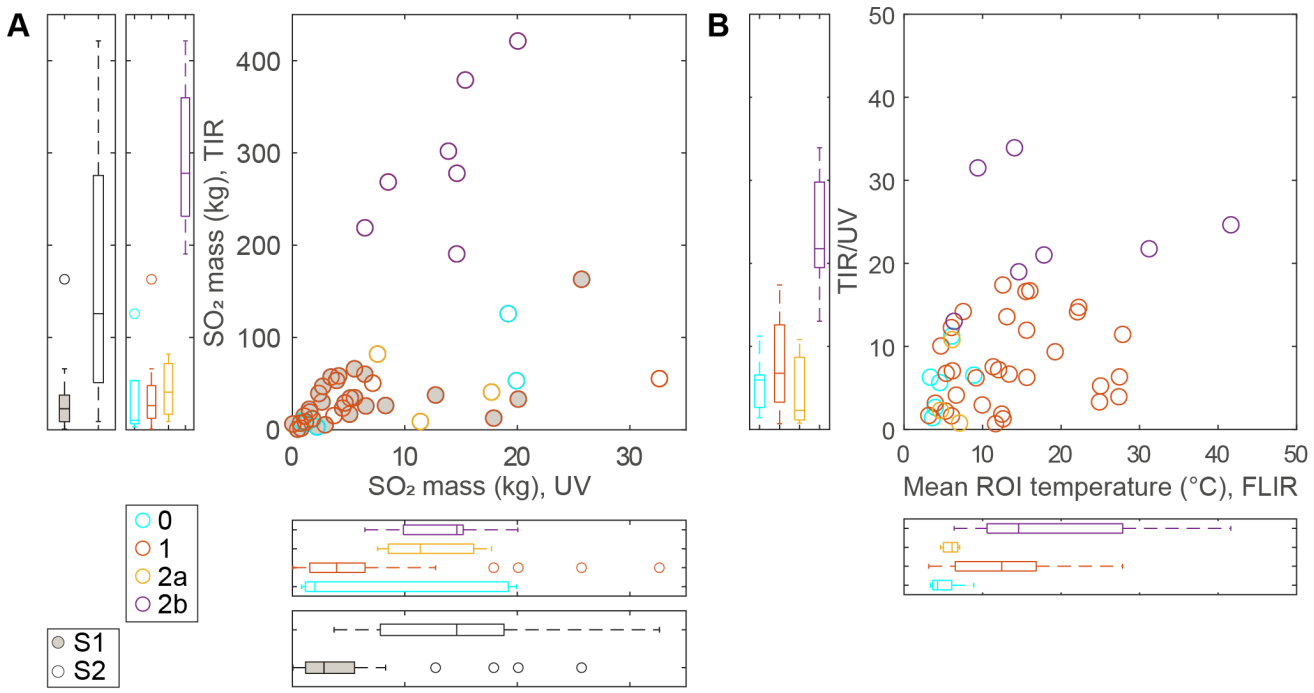

Figure 7: Scatter plots illustrating the correlation between [A] the explosion's peak SO_2 mass estimated by the UV and TIR cameras and [B] their ratio TIR/UV versus explosion Mean ROI temperature (peak value). For each scatterplot, the boxplots display the median, interquartile range, minimum and maximum values of the quantities in the horizontal and vertical axes, categorized by vent (S1 or S2) and explosion type (0, 1, 2a, 2b, see Table 2).

–Article in Press–

set, while lower-emissivity, particle-free, Type 0 explosions exhibit closer UV–TIR agreement.

Hence, the primary driver of the amplitude mismatch between TIR and UV datasets is the uncorrected effect of ash content and high-temperature material on TIR measurements (Figure 5C): ash particles, emitting in the thermal infrared spectrum, are misinterpreted by the TIR retrieval algorithm as additional SO_2 contributing to the systematic overestimation of SO_2 mass in the TIR data. This effect is difficult to correct without independent constraints on particle size, emissivity, concentration, and spatial distribution [e.g. Corradini et al. 2009]. Furthermore, hot ballistic bombs (prominent in Type 1 explosions), cause sharp temperature spikes that can dominate the radiative signal, further biasing TIR measurements and inflating SO_2 estimates—especially when falling within the region of interest [e.g. Prata and Bernardo 2009; 2014; Lopez et al. 2015].

In contrast, UV-based SO_2 retrievals are largely unaffected by temperature (Figure 5D), but they can be temporarily disturbed by ash, which causes radiative transfer effects attenuating UV signals. This interference is most pronounced during the first few seconds of an explosion, when the plume is densest and optically thickest [Kern et al. 2010; Tamburello et al. 2012]. At Stromboli, ash concentrations during Type 2b explosions were measured to range between 10^{-3} and 10^{-5} kg m^{-3} in the first seconds of explosions, followed by rapid dilution [Donnadieu et al. 2016]. This effect was evident in our measurements of Type 2b explosions, where the large volumes of ash at the onset of the explosive events caused a negative peak in the UV signal (Figure 2D). However, our explosion's peak masses have already been corrected for this effect, as the adopted SO_2 mass picking strategy excluded the negative peak (Figure 2D). This approach effectively removed the main source of underestimation due to concentrated ash, which would otherwise have led to a 3–15 % difference in the SO_2 mass estimate for Type 2b events. Residual interference from ash cannot be completely ruled out, but differences in underestimation among explosion types are minimised. The remaining baseline uncertainty—caused by radiative transfer effects such as scattering by aerosols and ash—affects all measurements, including passive and active degassing as well as all explosion types; we consider this quantity, typically around 30 % [Kern et al. 2010], to represent the residual error affecting our UV data.

To summarise, the significant SO_2 mass differences found for 2b explosions likely results from the opposite combined response of the two sensors. Since the residual uncertainty from UV measurements is relatively small (~30 %) compared to the much larger discrepancies observed for explosive events (Figure 7, Table 2), we attribute the majority of the mismatch to the TIR retrieval algorithm, which does not fully correct for particle-related effects. This highlights that our ground-based TIR technique is currently unsuitable for SO_2 retrieval during high-temperature, ash-rich explosive activity and requires ash and temperature-based correction. Conversely, during passive degassing the methods yield comparable SO_2 mass values. These findings underscore the complexities of SO_2 retrieval from different techniques and emphasize the necessity of inte-

–Article in Press–

grating multiple approaches for a more comprehensive assessment of volcanic gas emissions. The poor point-by-point correlation analysis observed between TIR and UV, highlight the importance of considering environmental and methodological factors when interpreting SO_2 data, particularly in dynamic explosive settings like Stromboli, where ash content, particle distribution, and localized temperature spikes limit the reliability of TIR–UV correlation.

5.2 SO_2 emissions comparison with previous studies

Given the above discussed limitation on TIR-based SO_2 masses, UV-based measurements offer a more conservative and reliable estimate of explosive SO_2 output for direct comparison with prior studies. The explosion type classification reveals a clear increase in UV-retrieved SO_2 mass with ash content. Ash-free explosions (Type 0 and 1) show the lowest SO_2 emissions (UV median 2.0–3.9 kg), while ash-rich explosions (Type 2a–b) show the highest (UV median 11.4–14.6 kg). Overall, our UV-measured explosion masses of 1–33 kg align well with previous findings at Stromboli, reporting SO_2 explosive masses between 2 and 55 kg [Mori and Burton 2009; Tamburello et al. 2012; Barnie et al. 2015; Delle Donne et al. 2017; Delle Donne et al. 2022]. This consistency, despite the differences in methodologies and observational conditions, supports the robustness of our UV-based retrievals. A broader comparison with Ilanko et al. [2020], who reported Strombolian explosion SO_2 masses at Yasur volcano between 8–81 kg (mean of 32 kg), suggests similar active degassing styles, albeit at different volcanoes. Lastly, our UV data are consistent with observations at Etna during mild Strombolian activity, where SO_2 masses ranged from 0.1 to 14 kg [Bani and Lardy 2007].

Our study allows a distinction between passive and active degassing, crucial in interpreting SO_2 emissions at Stromboli. During passive degassing—defined as the continuous emission of volcanic gases outside explosive phases—both UV and TIR methods recorded consistent background SO_2 emissions, with masses per frame ranging 3–7 kg and 1–8 kg (IQR values), for UV and TIR respectively (Table 2). Specifically, these values represent the integrated SO_2 mass within the defined ROI for a single frame, effectively giving an instantaneous plume mass (i.e. the sum of pixel values converted to mass). Converting these data to fluxes could be done by calculating the frame by frame change in integrated mass over time ($\Delta m/\Delta t$). In practice, this method can be noisy and inaccurate unless mass is steadily increasing or decreasing in the ROI. To better compare literature data on passive degassing, it is more appropriate to consider, rather than discrete SO_2 masses, the SO_2 flux obtained by integrating the SO_2 column densities along a transect located inside the ROI, approximately 10 m above the crater terrace (See Supplementary Material 1 Figure S3B) and multiplying by an assumed average plume rise speed of ~2 $m\,s^{-1}$ [following Tamburello et al. 2012]. Explosive periods were excluded from the analysis to isolate passive degassing. Under these conditions, UV and TIR data provide median SO_2 fluxes of 0.4 $kg\,s^{-1}$ (IQR: 0.2–0.6) and 0.5 $kg\,s^{-1}$ (IQR: 0.1–2.1), respectively. These values are consistent with previously reported background SO_2 fluxes for Stromboli under passive degassing conditions [0.2–0.7 $kg\,s^{-1}$; Tamburello et al. 2012; Burton et al. 2015; Delle Donne et al. 2017; Delle Donne et al. 2022], confirming that both UV and TIR techniques provide similar SO_2 estimates during passive degassing, especially in the absence of thermal and particulate interference from explosions.

5.3 Strengths and limitations of observation methods

Our findings highlight that both UV camera and the VIRSO_2 TIR-based camera have distinct advantages and limitations. The UV camera provides high-temporal-resolution measurements, making it particularly effective for capturing active degassing during explosive events. The UV method is not affected by temperature variations, ensuring more stable SO_2 retrievals regardless of the thermal conditions at the vent. Potential underestimations in the vicinity of the vent due to ash content can be mitigated using our proposed strategy. Furthermore, because UV cameras rely on sunlight passing through the plume, they require proper positioning and time of day to ensure strong SO_2 signals and minimizing glare or low contrast. Another limitation, specific to the camera system used here, is the small FOV. Despite these restrictions, its high frame rate makes it well-suited for monitoring dynamic volcanic activity in an environment like Stromboli, where rapid gas pulses are common.

The VIRSO_2 based TIR camera system offers the advantage of day and night operation, making it particularly useful for continuous long-term monitoring. However, its low acquisition frequency limits its ability to detect short-lived emissions associated with Strombolian explosions. Currently, the main limitation is that the retrieval algorithm does not correct for ash and temperature spikes that dominate the radiative signal. A new algorithm addressing these effects will make the system suitable for Strombolian explosions. Since the primary goal of our study was to compare the two retrieval techniques under controlled conditions, we adopted the method based on the near-vent ROI for SO_2 mass retrieval. While this approach inevitably emphasized the overestimation in the TIR data, it enabled a spatially and temporally synchronized comparison with the UV camera, ensuring that discrepancies between the two signals were attributable solely to instrumental differences rather than variable analysis setting.

The more conventional SO_2 flux-based approach which involves integrating the column amounts along a plume-crossing transect and multiplying by an assumed plume velocity, could in principle optimize the performance of each instrument, however, it requires different analysis settings for each system. As a test, we applied this method by considering the same UV transect near the vent (~10 m) to maximize the signal detectability and a TIR transect placed higher in the plume (~500 m, Supplementary Material 1 Figure S4), to reduce temperature-related biases. The assumed plume velocities were ~20–40 $m\,s^{-1}$ for the UV data (based on the interquartile range of measured explosion speeds; Figure 3B) and ~2–5 $m\,s^{-1}$ for the TIR data (estimated from buoyant rise observations at that height).

While this method did result in reduced discrepancies between SO_2 masses (Supplementary Material 1 Figure S4A), the TIR still overestimated SO_2 by a factor of 3–4. Moreover,

–Article in Press–

the flux-based method introduced several additional sources of uncertainty:

1. Velocity assumptions varied substantially between instruments and were not directly measured; in particular, applying a constant velocity to the UV data, while improving results during explosive phases, produced unrealistically high fluxes during passive degassing periods;

2. Spatial and temporal misalignment between the two transects complicated the comparison, as each instrument was observing different parts of the plume at different times;

3. Finally, mass conservation with elevation is not guaranteed, as explosive plumes are subject to rapid lateral spreading, buoyancy effects, and mixing with ambient air, which can cause a portion of the SO_2 to disperse or exit the field of view before TIR detection.

This last issue was particularly pronounced for the small, short-lived explosive plumes studied here, which often did not reach the TIR transect.

In light of these limitations, we find that the ROI-based mass retrieval approach, despite emphasizing TIR's known thermal biases, provided a more robust and consistent comparison under our observational conditions. At present, the TIR method remains more suitable for passive degassing measurements or when used in regions of the plume where temperatures and particle concentrations are low, minimizing related biases [Guerrieri et al. 2025].

5.4 Implications for future monitoring

While UV and TIR techniques both capture volcanic emissions, they respond differently: UV tends to underestimate SO_2 due to ash induced-scattering , whereas the current TIR dual-camera system is unable to completely correct for thermal radiation and scattering from ash and aerosols contamination overestimating it (up to one order of magnitude) due to spectral interference. This highlights the need to improve TIR SO_2 retrieval methods, to account for thermal contamination. A new correction approach is in development, building on experience with satellite-based TIR retrievals [Corradini et al. 2009].

Future improvements should address not only ash contamination but also thermal contrast in TIR data. Using multichannel thermal imagery can help quantify temperature differences, enabling correction of narrowband SO_2 retrievals—following previous methods that used the 8.6 µm channel for SO_2, 11–12 µm channels for ash, and the 10 µm channel, minimally affected by water vapor, for plume temperature [Prata and Bernardo 2009; 2014; Lopez et al. 2015]. Further, the automation of data acquisition and transmission is already under development, with testing expected soon.

We are also developing an optical flow algorithm using UV and high-speed thermal imagery to track the time-resolved velocity of both gas and solid plume components. Once these tools are refined, new co-located, time-synchronized UV–TIR acquisitions should be prioritized for better cross-validation. Ash-free or passive degassing conditions offer the most reliable calibration data and should guide algorithm development. Future campaigns should also integrate supporting data—like wind profiles and atmospheric temperatures—to better constrain plume dynamics and radiative effects. These enhancements will ultimately improve SO_2 flux estimates in both explosive and quiescent scenarios.

6 Conclusions

This study presents a comparison of ground-based UV and TIR retrievals of SO_2 mass during Strombolian activity at Stromboli volcano, highlighting the strengths and limitations of each technique. Both methods showed a synchronized response to SO_2 emission peaks, with correlation improving over minutes-long intervals compared to hours-long periods, but significant discrepancies exist, especially during ash-rich explosions due to their differing sensitivities to plume composition and radiative effects.

UV cameras, with their high temporal resolution, excel at capturing active degassing but are limited to daylight operation and constrained by solar geometry and optical depth effects. TIR measurements, on the other hand, provide continuous day-night observations but are strongly affected by the intertwined effects of explosion temperature and ash content, which together influence radiative transfer, leading to systematic overestimations of SO_2 mass, especially in ash-dominated explosions.

Despite these challenges, UV-based SO_2 retrievals in this study are consistent with previous findings at persistently active volcanoes, confirming their reliability for both explosive SO_2 quantification and passive degassing with only limited underestimation in ash-rich plumes. Once the TIR model is refined to account for temperature and ash effects, an integrated UV-TIR approach is recommended to optimize SO_2 monitoring in volcanic settings, ensuring a more comprehensive assessment of both explosive and passive degassing.

Author Contributions

EDB: data acquisition, methodology, analysis, writing – original draft, funding. EB: data acquisition, methodology, analysis, writing – original draft. LG: data acquisition, methodology, analysis, writing – review & editing. GT: software, methodology, writing – review & editing. SC: analysis, writing – review & editing. LM, FP, DS, JT: data acquisition. PS: data acquisition, funding. All authors approved the final manuscript.

Acknowledgements

All the authors received funding from "Progetto INGV Pianeta Dinamico - Sub-project VT_DYNAMO 2023 (DYNAmics of eruptive phenoMena at basaltic vOlcanoes), CUP D53J19000170001 - funded by Italian Ministry MIUR (Fondo Finalizzato al rilancio degli investimenti delle amministrazioni centrali dello Stato e allo sviluppo del Paese, legge 145/2018). EDB, EB, FP, PS, JT also benefited from funds from the European Union - Next-Generation EU - National Recovery and Resilience Plan (NRRP) – MISSION 4 COMPONENT 2, INVESTMENT No. 1.1, CALL PRIN 2022 D.D. 104 02-02-2022 – (PROVES: an integrated PetRO-Volcanological monitoring approach applied to Mt. Etna and Stromboli - 2022N4FBAA - CUP D53D23004780006) and by the INGV Departmental

–Article in Press–

Strategic Projects UNO (UNderstanding the Ordinary to forecast the extraordinary: An integrated approach for studying and interpreting the explosive activity at Stromboli volcano, CUP D59C19000140005).

Data Availability

Relevant data for this study are available in the Supplementary Material files accessible in the online version of this article. Unprocessed data can be provided upon request.

Copyright Notice

© The Author(s) 2025. This article is distributed under the terms of the Creative Commons Attribution 4.0 International License, which permits unrestricted use, distribution, and reproduction in any medium, provided you give appropriate credit to the original author(s) and the source, provide a link to the Creative Commons license, and indicate if changes were made.

References

Aiuppa, A., G. Lo Bue Trisciuzzi, S. Alparone, M. Bitetto, M. Coltelli, D. Delle Donne, G. Ganci, and E. Pecora (2023). "A SO_2 flux study of the Etna volcano 2020–2021 paroxysmal sequences". *Frontiers in Earth Science* 11. DOI: 10.3389/feart.2023.1115111.

Andronico, D., E. Del Bello, C. D'Oriano, P. Landi, F. Pardini, P. Scarlato, M. de'Michieli Vitturi, J. Taddeucci, A. Cristaldi, F. Ciancitto, F. Pennacchia, T. Ricci, and F. Valentini (2021). "Uncovering the eruptive patterns of the 2019 double paroxysm eruption crisis of Stromboli volcano". *Nature Communications* 12(1). DOI: 10.1038/s41467-021-24420-1.

Bani, P. and M. Lardy (2007). "Sulphur dioxide emission rates from Yasur volcano, Vanuatu archipelago". *Geophysical Research Letters* 34(20). DOI: 10.1029/2007gl030411.

Barnie, T., M. Bombrun, M. R. Burton, A. Harris, and G. Sawyer (2015). "Quantification of gas and solid emissions during Strombolian explosions using simultaneous sulphur dioxide and infrared camera observations". *Journal of Volcanology and Geothermal Research* 300, pages 167–174. DOI: 10.1016/j.jvolgeores.2014.10.003.

Berk, A., G. P. Anderson, P. K. Acharya, L. S. Bernstein, L. Muratov, J. Lee, M. J. Fox, S. M. Adler-Golden, J. H. Chetwynd, M. L. Hoke, R. B. Lockwood, T. W. Cooley, and J. A. Gardner (2005). "MODTRAN5: a reformulated atmospheric band model with auxiliary species and practical multiple scattering options". *Multispectral and Hyperspectral Remote Sensing Instruments and Applications II, Proceedings*. Volume 5655. Fourth International Asia-Pacific Environmental Remote Sensing Symposium 2004: Remote Sensing of the Atmosphere, Ocean, Environment, and Space. Honolulu, Hawai'i: SPIE, page 13. DOI: 10.1117/12.578758.

Burton, M., G. Salerno, L. D'Auria, T. Caltabiano, F. Murè, and R. Maugeri (2015). "SO 2 flux monitoring at Stromboli with the new permanent INGV SO 2 camera system: A comparison with the FLAME network and seismological data". *Journal of Volcanology and Geothermal Research* 300, pages 95–102. DOI: 10.1016/j.jvolgeores.2015.02.006.

Campion, R., H. Delgado-Granados, and T. Mori (2015). "Image-based correction of the light dilution effect for SO 2 camera measurements". *Journal of Volcanology and Geothermal Research* 300, pages 48–57. DOI: 10.1016/j.jvolgeores.2015.01.004.

Coppola, D., M. Laiolo, C. Cigolini, D. Delle Donne, and M. Ripepe (2016). "Enhanced volcanic hot-spot detection using MODIS IR data: results from the MIROVA system". *Geological Society, London, Special Publications* 426(1), pages 181–205. DOI: 10.1144/sp426.5.

Corradini, S., L. Guerrieri, H. Brenot, L. Clarisse, L. Merucci, F. Pardini, A. J. Prata, V. J. Realmuto, D. Stelitano, and N. Theys (2021). "Tropospheric Volcanic SO_2 Mass and Flux Retrievals from Satellite. The Etna December 2018 Eruption". *Remote Sensing* 13(11), page 2225. DOI: 10.3390/rs13112225.

Corradini, S., L. Merucci, A. J. Prata, and A. Piscini (2010). "Volcanic ash and SO_2 in the 2008 Kasatochi eruption: Retrievals comparison from different IR satellite sensors". *Journal of Geophysical Research: Atmospheres* 115(D2). DOI: 10.1029/2009jd013634.

Corradini, S., L. Merucci, and A. J. Prata (2009). "Retrieval of SO_2 from thermal infrared satellite measurements: correction procedures for the effects of volcanic ash". *Atmospheric Measurement Techniques* 2(1), pages 177–191. DOI: 10.5194/amt-2-177-2009.

Delle Donne, D., G. Tamburello, A. Aiuppa, M. Bitetto, G. Lacanna, R. D'Aleo, and M. Ripepe (2017). "Exploring the explosive-effusive transition using permanent ultraviolet cameras". *Journal of Geophysical Research: Solid Earth* 122(6), pages 4377–4394. DOI: 10.1002/2017jb014027.

Delle Donne, D., E. Lo Coco, M. Bitetto, F. P. La Monica, G. Lacanna, J. Lages, M. Ripepe, G. Tamburello, and A. Aiuppa (2022). "Spatio-temporal changes in degassing behavior at Stromboli volcano derived from two co-exposed SO_2 camera stations". *Frontiers in Earth Science* 10. DOI: 10.3389/feart.2022.972071.

Donnadieu, F., V. Freret-Lorgeril, J. Delanoë, J.-P. Vinson, F. Peyrin, C. Hervier, C. Caudoux, J. Van Baelen, and T. Latchimy (2016). "Multifrequency radar imaging of ash plumes: an experiment at Stromboli". Volume 18. EGU2016-15038-1. EGU General Assembly. Geophysical Research Abstracts.

Gaudin, D., J. Taddeucci, P. Scarlato, A. Harris, M. Bombrun, E. Del Bello, and T. Ricci (2017). "Characteristics of puffing activity revealed by ground-based, thermal infrared imaging: the example of Stromboli Volcano (Italy)". *Bulletin of Volcanology* 79(3). DOI: 10.1007/s00445-017-1108-x.

Guerrieri, L., S. Corradini, L. Merucci, D. Stelitano, F. Prata, L. Lambertucci, C. Naranjo, and R. Biondi (2025). "A novel simplified ground-based thermal infrared (TIR) system for volcanic plume geometry, SO_2 columnar abundance, and flux retrievals". *Atmospheric Measurement Techniques* 18(19), pages 5281–5297. DOI: 10.5194/amt-18-5281-2025.

Harris, A. and M. Ripepe (2007). "Temperature and dynamics of degassing at Stromboli". *Journal of Geophysical Research: Solid Earth* 112(B3). DOI: 10.1029/2006jb004393.

–Article in Press–

Hersbach, H., B. Bell, P. Berrisford, G. Biavati, A. Horányi, J. Muñoz Sabater, J. Nicolas, C. Peubey, R. Radu, I. Rozum, D. Schepers, A. Simmons, C. Soci, D. Dee, and J.-N. Thépaut (2023). "ERA5 hourly data on pressure levels from 1940 to present". *Copernicus Climate Change Service (C3S) Climate Data Store (CDS)*. DOI: 10.24381/CDS.BD0915C6. [Dataset].

Ilanko, T., T. D. Pering, T. C. Wilkes, J. Woitischek, R. Dâ€™Aleo, A. Aiuppa, A. J. S. McGonigle, M. Edmonds, and E. Garaebiti (2020). "Ultraviolet Camera Measurements of Passive and Explosive (Strombolian) Sulphur Dioxide Emissions at Yasur Volcano, Vanuatu". *Remote Sensing* 12(17), page 2703. DOI: 10.3390/rs12172703.

Kantzas, E. P., A. J. S. McGonigle, G. Tamburello, A. Aiuppa, and R. G. Bryant (2010). "Protocols for UV camera volcanic SO_2 measurements". *Journal of Volcanology and Geothermal Research* 194(1–3), pages 55–60. DOI: 10.1016/j.jvolgeores.2010.05.003.

Kearney, C. S., K. Dean, V. J. Realmuto, I. M. Watson, J. Dehn, and F. Prata (2008). "Observations of SO_2 production and transport from Bezymianny volcano, Kamchatka using the MODerate resolution Infrared Spectroradiometer (MODIS)". *International Journal of Remote Sensing* 29(22), pages 6647–6665. DOI: 10.1080/01431160802168392.

Kearney, C. S. and I. M. Watson (2009). "Correcting satellite-based infrared sulfur dioxide retrievals for the presence of silicate ash". *Journal of Geophysical Research: Atmospheres* 114(D22). DOI: 10.1029/2008jd011407.

Kern, C., T. Deutschmann, L. Vogel, M. Wöhrbach, T. Wagner, and U. Platt (2010). "Radiative transfer corrections for accurate spectroscopic measurements of volcanic gas emissions". *Bulletin of Volcanology* 72(2), pages 233–247. DOI: 10.1007/s00445-009-0313-7.

Leduc, L., L. Gurioli, A. Harris, L. Colò, and E. F. Rose-Koga (2015). "Types and mechanisms of strombolian explosions: characterization of a gas-dominated explosion at Stromboli". *Bulletin of Volcanology* 77(1). DOI: 10.1007/s00445-014-0888-5.

Lo Bue Trisciuzzi, G., A. Aiuppa, G. Salerno, M. Bitetto, L. Curcio, L. Innocenti, G. Lacanna, J. P. Nogueira Lages, F. M. Lo Forte, S. R. Maugeri, F. MurÃ¨, P. Principato, M. Ripepe, A. Vitale, and D. Delle Donne (2024). "Improved volcanic SO_2 flux records from integrated scanning-DOAS and UV Camera observations." *Journal of Volcanology and Geothermal Research* 455, page 108207. DOI: 10.1016/j.jvolgeores.2024.108207.

Lopez, T., H. E. Thomas, A. J. Prata, A. Amigo, D. Fee, and D. Moriano (2015). "Volcanic plume characteristics determined using an infrared imaging camera". *Journal of Volcanology and Geothermal Research* 300, pages 148–166. DOI: 10.1016/j.jvolgeores.2014.12.009.

Marzano, F. S., S. Corradini, L. Mereu, A. Kylling, M. Montopoli, D. Cimini, L. Merucci, and D. Stelitano (2018). "Multi-satellite Multisensor Observations of a Sub-Plinian Volcanic Eruption: The 2015 Calbuco Explosive Event in Chile". *IEEE Transactions on Geoscience and Remote Sensing* 56(5), pages 2597–2612. DOI: 10.1109/tgrs.2017.2769003.

Mereu, L., F. S. Marzano, C. Bonadonna, G. Lacanna, M. Ripepe, and S. Scollo (2023). "Automatic Early Warning to Derive Eruption Source Parameters of Paroxysmal Activity at Mt. Etna (Italy)". *Remote Sensing* 15(14), page 3501. DOI: 10.3390/rs15143501.

Mori, T. and M. Burton (2009). "Quantification of the gas mass emitted during single explosions on Stromboli with the SO_2 imaging camera". *Journal of Volcanology and Geothermal Research* 188(4), pages 395–400. DOI: 10.1016/j.jvolgeores.2009.10.005.

Patrick, M. R., A. J. L. Harris, M. Ripepe, J. Dehn, D. A. Rothery, and S. Calvari (2007). "Strombolian explosive styles and source conditions: insights from thermal (FLIR) video". *Bulletin of Volcanology* 69(7), pages 769–784. DOI: 10.1007/s00445-006-0107-0.

Prata, A. J. and C. Bernardo (2014). "Retrieval of sulfur dioxide from a ground-based thermal infrared imaging camera". *Atmospheric Measurement Techniques* 7(9), pages 2807–2828. DOI: 10.5194/amt-7-2807-2014.

Prata, A. J. and I. Grant (2001). "Determination of mass loadings and plume heights of volcanic ash clouds from satellite data". *CSIRO Atmospheric Research Technical Paper* (48). DOI: 10.13140/RG.2.1.4405.2327.

Prata, A. and C. Bernardo (2009). "Retrieval of volcanic ash particle size, mass and optical depth from a ground-based thermal infrared camera". *Journal of Volcanology and Geothermal Research* 186(1–2), pages 91–107. DOI: 10.1016/j.jvolgeores.2009.02.007.

Prata, F., S. Corradini, R. Biondi, L. Guerrieri, L. Merucci, A. Prata, and D. Stelitano (2024). "Applications of Ground-Based Infrared Cameras for Remote Sensing of Volcanic Plumes". *Geosciences* 14(3), page 82. DOI: 10.3390/geosciences14030082.

Rowell, C. R., A. M. Jellinek, and J. T. Gilchrist (2023). "Tracking Eruption Column Thermal Evolution and Source Unsteadiness in Ground-Based Thermal Imagery Using Spectral-Clustering". *Geochemistry, Geophysics, Geosystems* 24(11). DOI: 10.1029/2022gc010845.

Sahetapy-Engel, S. T. and A. J. L. Harris (2009). "Thermal-image-derived dynamics of vertical ash plumes at Santiaguito volcano, Guatemala". *Bulletin of Volcanology* 71(7), pages 827–830. DOI: 10.1007/s00445-009-0284-8.

Simons, B. C., S. J. Cronin, J. D. Eccles, A. D. Jolly, E. Garaebiti, and S. Cevuard (2020). "Spatiotemporal variations in eruption style and magnitude at Yasur volcano, Vanuatu: part 2â€"extending Strombolian eruption classifications". *Bulletin of Volcanology* 82(11). DOI: 10.1007/s00445-020-01404-5.

Taddeucci, J., P. Scarlato, D. Andronico, T. Ricci, R. Civico, E. Del Bello, L. Spina, L. D'Auria, M. Asensio-Ramos, D. Calvo, E. Padrón, P. A. Hernández, and N. M. Pérez (2023). "The Explosive Activity of the 2021 Tajogaite Eruption (La Palma, Canary Islands, Spain)". *Geochemistry, Geophysics, Geosystems* 24(6). DOI: 10.1029/2023gc010946.

Taddeucci, J., P. Scarlato, A. Capponi, E. Del Bello, C. Cimarelli, D. M. Palladino, and U. Kueppers (2012). "High-

–Article in Press–

–Article in Press–

speed imaging of Strombolian explosions: The ejection velocity of pyroclasts". *Geophysical Research Letters* 39(2). DOI: 10.1029/2011gl050404.

Taddeucci, J., P. Scarlato, E. Del Bello, G. Tamburello, and D. Gaudin (2018). "Eruptions from UV to TIR: multispectral high-speed imaging of explosive volcanic activity". *Light, Energy and the Environment 2018 (E2, FTS, HISE, SOLAR, SSL)*. Optica Publishing Group, HM2C.2. DOI: 10.1364/HISE.2018.HM2C.2.

Tamburello, G., A. Aiuppa, E. P. Kantzas, A. J. S. McGonigle, and M. Ripepe (2012). "Passive vs. active degassing modes at an open-vent volcano (Stromboli, Italy)". *Earth and Planetary Science Letters* 359–360, pages 106–116. DOI: 10.1016/j.epsl.2012.09.050.

Tamburello, G., E. P. Kantzas, A. J. S. McGonigle, and A. Aiuppa (2011). "Vulcamera: a program for measuring volcanic SO_2 using UV cameras". *Annals of Geophysics* 54(2). DOI: 10.4401/ag-5181.

Varnam, M., M. Burton, B. Esse, G. Salerno, R. Kazahaya, and M. Ibarra (2021). "Two Independent Light Dilution Corrections for the SO_2 Camera Retrieve Comparable Emission Rates at Masaya Volcano, Nicaragua". *Remote Sensing* 13(5), page 935. DOI: 10.3390/rs13050935.

Watson, I., V. Realmuto, W. Rose, A. Prata, G. Bluth, Y. Gu, C. Bader, and T. Yu (2004). "Thermal infrared remote sensing of volcanic emissions using the moderate resolution imaging spectroradiometer". *Journal of Volcanology and Geothermal Research* 135(1–2), pages 75–89. DOI: 10.1016/j.jvolgeores.2003.12.017.

–Article in Press–

–Article in Press–